

A positive meshless finite difference scheme for scalar conservation laws with adaptive artificial viscosity driven by fault detection

Cesare Bracco^a, Oleg Davydov^b, Carlotta Giannelli^a, Alessandra Sestini^a

^a *Dipartimento di Matematica e Informatica “U. Dini”, Università degli Studi di Firenze,
Viale Morgagni 67a, 50134 Florence, Italy*

^b *Department of Mathematics, Justus Liebig University Giessen, Arndtstrasse 2, 35392 Giessen, Germany*

March 16, 2025

Abstract

We present a meshless finite difference method for multivariate scalar conservation laws that generates positive schemes satisfying a local maximum principle on irregular nodes and relies on artificial viscosity for shock capturing. Coupling two different numerical differentiation formulas and the adaptive selection of the sets of influence allows to meet a local CFL condition without any *a priori* time step restriction. The artificial viscosity term is chosen in an adaptive way by applying it only in the vicinity of the sharp features of the solution identified by an algorithm for fault detection on scattered data. Numerical tests demonstrate a robust performance of the method on irregular nodes and advantages of adaptive artificial viscosity. The accuracy of the obtained solutions is comparable to that for standard monotone methods available only on Cartesian grids.

Keywords: Conservation laws, Meshless finite difference methods, Adaptive artificial viscosity, Minimal numerical differentiation formulas, Fault detection

1. Introduction

Meshless methods discretize partial differential equations on irregular nodes in space without creating a grid or mesh [Suchde et al. \(2022\)](#). This allows to distribute the degrees of freedom in the most flexible way and rapidly rearrange them if needed as time evolves, without meshing or re-meshing, and thus eliminating a major time consuming and often algorithmically difficult step in numerical simulations. Especially, meshless finite difference methods, based on polynomials or radial basis functions, see for example [Oñate et al. \(1996\)](#); [Fornberg and Flyer \(2015\)](#); [Jacquemin et al. \(2020\)](#), attract increasing attention of engineers and mathematicians as a general purpose numerical technique that combines the basic simplicity and high accuracy inherited from the classical finite difference method with full spatial flexibility.

Numerical approximation of nonlinear multivariate hyperbolic conservation laws that model compressible fluid flow is an area where these methods have a lot to offer because of the complexity of the solutions, with shock discontinuities developing and moving in time. A major challenge for developing effective schemes of this type is that the standard multivariate finite difference schemes for conservation laws are obtained by applying univariate methods in a dimension-by-dimension fashion, see e.g. [Hesthaven \(2018\)](#). Univariate numerical fluxes or Riemann solvers may also be naturally applied in the normal direction to the element interfaces in partition-based methods. However, exploiting such univariate structures is more difficult in the setting of meshless finite difference methods, and may lead to undesired restrictions on the node generation or selection of sets of influence, reducing the natural geometric flexibility of these methods. Nevertheless, several approaches exploiting an edge-based connectivity structure by either borrowing it from a mesh or generating it in a meshless cloud of nodes, can be found in [Löhner et al. \(2002\)](#); [Sridar and Balakrishnan](#)

Email addresses: cesare.bracco@unifi.it (Cesare Bracco), oleg.davydov@math.uni-giessen.de (Oleg Davydov), carlotta.giannelli@unifi.it (Carlotta Giannelli), alessandra.sestini@unifi.it (Alessandra Sestini)

(2003); Shu et al. (2005); Praveen and Deshpande (2007); Ortega et al. (2009); Katz and Jameson (2012, 2010); Huh et al. (2018).

The idea that the stability of a numerical scheme in the vicinity of the shocks may be achieved with the help of an appropriate artificial viscosity term added to a central type scheme for the divergence goes back to von Neumann and Richtmyer (1950) for classical finite differences, and is a popular approach in the meshless finite difference methods, see in particular Batina (1993); Fornberg and Lehto (2011); Flyer et al. (2012); Shankar and Fogelson (2018); Tominec and Nazarov (2023). The viscosity term serves to enforce a stable eigenvalue spectrum of the discrete iterative scheme and also helps to correctly reproduce the shock movement thanks to the principle of vanishing viscosity. Ghosh and Deshpande (1995); Kuhnert (2003); Li and Fan (2017); Seifarth (2017) pursue the same goals via upwind schemes, where the divergence at a node is discretized on neighboring nodes in the upstream half-space. In particular, for scalar conservation laws the artificial viscosity term or upwinding may be organized such that the weights of the scheme are *positive* if the neighborhoods of all nodes are well-balanced. Then the numerical approximation of the state variable at each node is a convex combination of the state variables of the previous time step at neighboring nodes if the time step is sufficiently small, which ensures local maximum principle and hence the stability. Note that in the meshless setting numerical results in the literature are often presented for nodes obtained by highly optimized algorithms based for example on the minimization of the repulsion energy applied to simple domains such as the square. On the other hand, the full advantage of meshless methods may only be realized if the methods are sufficiently robust to guarantee stability on rather irregular nodes obtained by inexpensive algorithms, see Suchde et al. (2022).

Numerical schemes for bivariate scalar conservation laws that are guaranteed to be positive on irregular nodes have been suggested in Fürst and Sonar (2001) and Yin et al. (2011). In this approach the individual weights of a numerical differentiation formula for the divergence on irregular nodes are first modified to eliminate the unwanted signs, and then an artificial viscosity term is added to restore the first order consistency of the formula. Therefore the amount of local viscosity is driven by the stability goal, and only by chance may help the shock capturing.

In this paper we suggest a positive meshless scheme on irregular nodes for scalar conservation laws with any number of independent variables that does not require any additional structures in the node sets, and employs artificial viscosity for shock capturing rather than enforcing positivity. The conservation law is discretized in the quasilinear formulation via numerical differentiation formulas for the gradient operator on irregular nodes by a polynomial local least squares scheme combining minimization of an error bound for numerical differentiation suggested in Davydov and Schaback (2018) with inequality constraints that ensure the positivity of the scheme. The solvability of the small local quadratic optimization problems arising from this approach is achieved by consecutive enlargements of the set of influence until it meets a local CFL condition (that is, the positivity of the central weight of the scheme). Therefore, no global CFL condition is needed, and no *a priori* time step restriction is used. Artificial viscosity term is chosen in a adaptive way by applying it only in the vicinity of the sharp features of the solution, in order to ensure shock capturing, which reduces the overall numerical dissipation. We identify the regions of discontinuity by the recent fault detection method of Bracco et al. (2019) designed for scattered data.

We test numerically three versions of our scheme (no artificial viscosity, constant or adaptive artificial viscosity) on irregular nodes for three bivariate benchmark problems: inviscid Burgers' equation with either smooth or discontinuous initial condition, and the rotating wave problem with a non-convex flux. In all cases solutions are non-oscillating as expected due to the positivity of the schemes. The shocks are reproduced by both methods that employ artificial viscosity, while the version with adaptive viscosity is less dissipative. The accuracy of our solutions is comparable to those obtained by classical monotone schemes on Cartesian grids, and mostly somewhat better, despite using irregular nodes.

We expect that our positive first order scheme may be complemented by high order discretizations in conjunction with limiters, ENO/WENO and further ideas known in the literature on conservation laws.

The structure of the paper is as follows. Section 2 introduces positive meshless finite difference schemes and discusses their stability, consistency and the role of the artificial viscosity term. Section 3 describes our algorithm for choosing the weights of the inequality constrained minimal numerical differentiation formulas for the space discretization of the conservation law and a viscosity term, which serves as the main tool to

ensure a local CFL condition and the positivity of the scheme. Section 4 presents our adaptive algorithm that determines the amount of local artificial viscosity for each node. In Section 5 we formulate three methods to obtain positive schemes that differ in how they handle the artificial viscosity. Numerical tests are presented in Section 6, and a conclusion is given in Section 7.

2. Positive meshless finite difference schemes for scalar conservation laws

In this paper we deal with the meshless numerical solution of a general scalar conservation law on a bounded domain $\Omega \subset \mathbb{R}^d$, $d \geq 2$. (However, as usual, a problem on a hyperrectangle with periodic boundary conditions may be interpreted as being posed on $\Omega = \mathbb{R}^d$.) Thus, the considered problem is modeled by the following PDE

$$u_t + \nabla_{\mathbf{x}} \cdot \mathbf{F}(u) = 0, \quad t \in (0, T), \quad \mathbf{x} = (x_1, \dots, x_d) \in \Omega, \quad (1)$$

where $\nabla_{\mathbf{x}} \cdot$ denotes the divergence operator in space and the PDE is endowed with suitable boundary conditions and with the initial condition

$$u(0, \mathbf{x}) = u_0(\mathbf{x}), \quad \mathbf{x} \in \Omega. \quad (2)$$

As usual, the unknown function $u : (0, T) \times \Omega \rightarrow \mathbb{R}$, $u = u(t, \mathbf{x})$, is called the *state variable*, and the given vector function $\mathbf{F} : \mathbb{R} \rightarrow \mathbb{R}^d$, $\mathbf{F}(u) = (F_1(u), \dots, F_d(u))$, with $F_i : \mathbb{R} \rightarrow \mathbb{R}$, $i = 1, \dots, d$, is the *flux*. We assume that \mathbf{F} is differentiable, so that the *conservative form* (1) of the equation may be replaced by the equivalent *quasilinear* equation

$$u_t + \mathbf{F}'(u) \nabla_{\mathbf{x}} u = 0, \quad (3)$$

where $\nabla_{\mathbf{x}}$ is the space gradient and $\mathbf{F}'(u) := (F'_1(u), \dots, F'_d(u))$. In particular, in the case when $\mathbf{F}(u) = u\mathbf{v}$, with \mathbf{v} denoting a nonvanishing constant vector in \mathbb{R}^d , we obtain the equation of the *constant linear transport*. For any conservation law (1), the state variable u is conserved with respect to time. In particular, for each $\mathbf{x}_0 \in \Omega$, u remains constantly equal to $u_0(\mathbf{x}_0)$ along the corresponding outgoing *characteristic line* $(t, \mathbf{x}(t))$, $t \geq 0$, of the $d + 1$ -dimensional t - \mathbf{x} space, where

$$\mathbf{x}(t) = t\mathbf{F}'(\hat{u}_0) + \mathbf{x}_0, \quad \hat{u}_0 = u_0(\mathbf{x}_0).$$

Clearly, the presence of characteristics implies first of all that every finite jump in u_0 is transported along the characteristics when time goes on. Furthermore, in the nonlinear case two characteristics may intersect and this implies that the strong solution of (1) is only well defined for sufficiently small T . For later times, discontinuities (shocks) may appear, even when u_0 is smooth, after which the equation gets many weak solutions, such that special efforts are required to identify a physically meaningful continuation of the state variable, so called *entropy solution*, see for example [Hesthaven \(2018\)](#).

Because of all these difficulties, sophisticated adaptive algorithms are needed in order to obtain satisfactory numerical approximations of challenging conservation law problems arising in applications. Therefore numerical methods capable to address these challenges must be in position to quickly refine, coarsen and rearrange the discretization of the spatial computational domain when time evolves. Even if mesh-based numerical techniques such as finite volume method or discontinuous Galerkin method possess a great deal of flexibility, they are often slowed down by the pitfalls of the meshing technology. Meshless methods, in particular meshless finite differences, that rely solely on nodes distributed irregularly in the space, without the need to connect them into meshes, provide a promising alternative.

A variety of numerical algorithms for conservation laws has been developed for mesh-based methods, in particular for the classical finite difference method. They include low order monotone methods, high order limiter-based schemes, as well as high order ENO and WENO type approaches. Typically methods based on finite differences are developed for the univariate case and then generalized to Cartesian grids by a dimension-by-dimension construction, which makes mesh adaptation difficult.

In this paper we suggest a genuinely multivariate positive scheme applicable on arbitrary irregular nodes. It relies on the meshless finite difference method and therefore requires no grids, triangulations or any other meshes connecting the nodes.

Let $X = \{\mathbf{x}_1, \dots, \mathbf{x}_N\} \subset \bar{\Omega}$ be an arbitrary finite set of discretization nodes, and $\Delta t > 0$ a step size in time. Note that the term $\mathbf{F}'(u)\nabla_{\mathbf{x}}u$ in (3) for each fixed \mathbf{x} is the directional derivative of u at \mathbf{x} ,

$$D_{\boldsymbol{\eta}}u(t, \mathbf{x}) = \frac{\partial u}{\partial \boldsymbol{\eta}}(t, \mathbf{x}) = \eta_1 \frac{\partial u}{\partial x_1}(t, \mathbf{x}) + \dots + \eta_d \frac{\partial u}{\partial x_d}(t, \mathbf{x})$$

in the direction $\boldsymbol{\eta} = \mathbf{F}'(u(t, \mathbf{x}))$, a vector with components $F'_1(u(t, \mathbf{x})), \dots, F'_d(u(t, \mathbf{x}))$. (Note that $\boldsymbol{\eta}$ is not normalized.) The approximate solution U is computed recursively by applying the Euler method in time and bivariate numerical differentiation formulas in space according to the rule

$$U(t + \Delta t, \mathbf{x}_i) = U(t, \mathbf{x}_i) - \Delta t \sum_{\mathbf{x}_j \in X_i} w_{ij} U(t, \mathbf{x}_j), \quad U(0, \mathbf{x}_i) = u_0(\mathbf{x}_i), \quad (4)$$

where X_i is a subset of X called the *influence set* of the node \mathbf{x}_i , and $w_{ij} \in \mathbb{R}$ are the *weights* of a numerical differentiation formula for the directional derivative at \mathbf{x}_i ,

$$D_{\boldsymbol{\eta}_i}f(\mathbf{x}_i) \approx \sum_{\mathbf{x}_j \in X_i} w_{ij}f(\mathbf{x}_j), \quad \boldsymbol{\eta}_i := \mathbf{F}'(U(t, \mathbf{x}_i)). \quad (5)$$

The influence set X_i is a small selection of nodes in the neighborhood of \mathbf{x}_i . We stress that in contrast to the classical finite difference method, the influence sets X_i are irregular and usually have different geometric shapes for different nodes \mathbf{x}_i . Hence, the weights w_{ij} have to be determined individually for each \mathbf{x}_i rather than being some scaled versions of a fixed stencil. Moreover, the weights also depend on the direction $\boldsymbol{\eta}_i$, therefore the weights w_{ij} , $j \in X_i$, are in general different for different i and different times.

Assuming without loss of generality that $\mathbf{x}_i \in X_i$ (otherwise we add \mathbf{x}_i to X_i and set $w_{ii} = 0$), we write (4) in the form

$$U(t + \Delta t, \mathbf{x}_i) = (1 - \Delta t w_{ii})U(t, \mathbf{x}_i) - \Delta t \sum_{\mathbf{x}_j \in X_i \setminus \{\mathbf{x}_i\}} w_{ij}U(t, \mathbf{x}_j).$$

The scheme (4) is said to be *positive* if the right hand side expression is a positive linear combination of $U(t, \mathbf{x}_j)$, $\mathbf{x}_j \in X_i$, that is, if

$$\Delta t w_{ii} \leq 1 \quad (6)$$

and

$$w_{ij} \leq 0, \quad \forall \mathbf{x}_j \in X_i \setminus \{\mathbf{x}_i\}. \quad (7)$$

Note that the weights w_{ij} may depend on $U(t, \mathbf{x}_i)$ since the direction $\boldsymbol{\eta}_i$ in (5) in general depends on it. Therefore, a positive scheme is not necessarily monotone, for which the right hand side of (4) would be required to be non-decreasing with respect to the values $U(t, \mathbf{x}_i)$ and $U(t, \mathbf{x}_j)$, $\mathbf{x}_j \in X_i$, of the approximate state variable at the previous time step, see [Hesthaven \(2018\)](#). Under additional assumption

$$\sum_{\mathbf{x}_j \in X_i} w_{ij} = 0 \quad (8)$$

the approximated value $U(t + \Delta t, \mathbf{x}_i)$ of the state variable at time $t + \Delta t$ is a convex combination of the values $U(t, \mathbf{x}_j)$, $\mathbf{x}_j \in X_i \cup \{\mathbf{x}_i\}$. Therefore the solution satisfies a *local maximum principle* in the form

$$\min_{\mathbf{x}_j \in X_i \cup \{\mathbf{x}_i\}} U(t, \mathbf{x}_j) \leq U(t + \Delta t, \mathbf{x}_i) \leq \max_{\mathbf{x}_j \in X_i \cup \{\mathbf{x}_i\}} U(t, \mathbf{x}_j), \quad (9)$$

which in particular implies the following inequalities for all time steps and all nodes \mathbf{x}_i

$$\min_{\mathbf{x} \in \bar{\Omega}} u_0(\mathbf{x}) \leq \min_{\mathbf{x}_j \in X} U(0, \mathbf{x}_j) \leq U(t, \mathbf{x}_i) \leq \max_{\mathbf{x}_j \in X} U(0, \mathbf{x}_j) \leq \max_{\mathbf{x} \in \bar{\Omega}} u_0(\mathbf{x}),$$

reproducing the maximum principle

$$\min_{\boldsymbol{\xi} \in \bar{\Omega}} u_0(\boldsymbol{\xi}) \leq u(t, \mathbf{x}) \leq \max_{\boldsymbol{\xi} \in \bar{\Omega}} u_0(\boldsymbol{\xi})$$

available for the entropy solution of the scalar conservation law (1), see for example Zhang et al. (2012). The local maximum principle (9) ensures the *stability* of the scheme and prevents unphysical behavior, such as artificial oscillations.

Positive schemes for scalar conservation laws originated in the classical upwind method by Courant et al. (1952). Positive and related *local extremum diminishing* schemes of higher order have been developed for mesh-based methods, see for example Jameson (1995); Guermond et al. (2014); Kuzmin (2020), as well as for meshless finite difference methods, using an underlying mesh or an edge-based connectivity structure Katz and Jameson (2012, 2010). Without imposing any connectivity of meshless discretization nodes, or their well-balanced distribution, positive first order methods have been suggested by Fürst and Sonar (2001); Yin et al. (2011) in the bivariate case $d = 2$. In contrast to the latter, our method described below is not restricted to two space dimensions, and does not use artificial viscosity to achieve positivity, which allows to devote it to the shock capturing.

We say that the scheme (4) is *consistent* in space, if the weights w_{ij} are chosen such that (5) is exact for all constant and linear polynomials,

$$D_{\eta_i} p(\mathbf{x}_i) = \sum_{\mathbf{x}_j \in X_i} w_{ij} p(\mathbf{x}_j) \quad \forall p \in \Pi_2^d, \quad (10)$$

where Π_q^d denotes the linear space of all polynomials of order at most q in d variables, that is of degree strictly less than q ,

$$\Pi_q^d = \text{span}\{\mathbf{x}^\alpha : \alpha \in \mathbb{Z}_+^d, |\alpha| < q\}, \quad \mathbf{x}^\alpha := x_1^{\alpha_1} \cdots x_d^{\alpha_d}, \quad |\alpha| := \alpha_1 + \cdots + \alpha_d.$$

Consistent schemes satisfy (8), which follows from the exactness of (5) for the constant $f = \mathbf{x}^0 \equiv 1$.

Stability and consistency of a positive scheme do not yet guarantee that the numerical solution $U(t, \mathbf{x})$ approximates the entropy solution rather than some other (unphysical) solution of (1) if shocks appear. A common approach to enforce this is based on the *principle of vanishing viscosity*, see for example Evans (2010), that says that the physical solution u of (1) is obtained as a limit for $\mu \rightarrow 0^+$ of the smooth solution u_μ of the parabolic initial value problem

$$u_t + \mathbf{F}'(u) \nabla_{\mathbf{x}} u = \mu \Delta_{\mathbf{x}} u, \quad u(0, \mathbf{x}) = u_{0,\mu}(\mathbf{x}), \quad \mu > 0, \quad (11)$$

where $u_{0,\mu}$ is a smooth approximation of u_0 converging to u_0 as $\mu \rightarrow 0^+$ in L_2 -norm. Therefore, we also choose a numerical differentiation formula for the space Laplacian $\Delta_{\mathbf{x}} = \frac{\partial^2}{\partial x_1^2} + \cdots + \frac{\partial^2}{\partial x_d^2}$ in the form

$$\Delta_{\mathbf{x}} f(\mathbf{x}_i) \approx \sum_{\mathbf{x}_j \in X_i} v_{ij} f(\mathbf{x}_j), \quad (12)$$

and require exactness for all quadratic polynomials,

$$\Delta_{\mathbf{x}} p(\mathbf{x}_i) = \sum_{\mathbf{x}_j \in X_i} v_{ij} p(\mathbf{x}_j) \quad \forall p \in \Pi_3^d. \quad (13)$$

The scheme (4) is modified by adding an *artificial viscosity* term multiplied by a small positive μ_i , which will be allowed to be chosen individually for each \mathbf{x}_i ,

$$U(t + \Delta t, \mathbf{x}_i) = U(t, \mathbf{x}_i) - \Delta t \sum_{\mathbf{x}_j \in X_i} w_{ij} U(t, \mathbf{x}_j) + \mu_i \Delta t \sum_{\mathbf{x}_j \in X_i} v_{ij} U(t, \mathbf{x}_j), \quad \mu_i > 0. \quad (14)$$

The modified scheme is positive if and only if

$$\Delta t (w_{ii} - \mu_i v_{ii}) \leq 1 \quad (15)$$

and

$$w_{ij} - \mu_i v_{ij} \leq 0, \quad \forall \mathbf{x}_j \in X_i \setminus \{\mathbf{x}_i\}. \quad (16)$$

Exactness of (12) for quadratic polynomials implies in particular exactness for constants, that is

$$\sum_{\mathbf{x}_j \in X_i} v_{ij} = 0, \quad (17)$$

hence the modified scheme retains the convex combination property and also satisfies the local maximum principle as soon as it is positive. Moreover, $\Delta p = 0$ for all linear polynomials, hence

$$\sum_{\mathbf{x}_j \in X_i} v_{ij} p(\mathbf{x}_j) = 0 \quad \forall p \in \Pi_2^d, \quad (18)$$

which implies that the scheme (14) written as (4) with w_{ij} replaced by $\tilde{w}_{ij} := w_{ij} - \mu_i v_{ij}$ remains a consistent discretization of (3) since

$$D_{\eta_i} p(\mathbf{x}_i) = \sum_{\mathbf{x}_j \in X_i} \tilde{w}_{ij} p(\mathbf{x}_j) \quad \forall p \in \Pi_2^d. \quad (19)$$

Note that we require exactness of (12) for quadratic polynomials, rather than only for linear polynomials, in order to ensure that $\sum_{\mathbf{x}_j \in X_i} v_{ij} U(t, \mathbf{x}_j)$ in the artificial viscosity term provides an approximation of the physical viscosity $\Delta_{\mathbf{x}} u$ at \mathbf{x}_i .

In what follows we obtain the weights w_{ij} and v_{ij} by solving for each \mathbf{x}_i a small quadratic optimization problem with linear equality and inequality constraints, see Section 3. It is clear that constraints (6) and (15) become less restrictive if Δt is smaller. We refer to (6) and (15) as *CFL conditions* even if we do not provide any bound for Δt that guarantees positivity and hence stability of the scheme, which is normally associated with CFL type conditions going back to Courant et al. (1928). Indeed, since we do not assume any regularity of the distribution of the nodes in X , it would not be efficient, for example, to first choose the weights w_{ij} and then take Δt so small that (6) is satisfied for all nodes \mathbf{x}_i .

Even if the choice of the time step Δt and the viscosity coefficients μ_i are in general problem dependent, and fine tuning them may significantly improve the results in the applications, it is important to take into account their natural rescaling depending on the size of the characteristic velocity. It is easy to see that the solution of (3) becomes $u(\gamma t, \mathbf{x})$ if $\mathbf{F}'(u)$ is replaced by $\gamma \mathbf{F}'(u)$, and the solution of (11) becomes $u(\gamma t, \mathbf{x})$ if $\mathbf{F}'(u)$ is replaced by $\gamma \mathbf{F}'(u)$, while μ is replaced by $\gamma \mu$, for any $\gamma > 0$. Therefore, in order to obtain the same behavior also in the discrete case, one needs to ensure that the discrete solution $U(t, \mathbf{x}_i)$ becomes $U(\gamma t, \mathbf{x}_i)$ under the same scaling of $\mathbf{F}'(u)$ and μ_i . Fortunately, this is easy to achieve for the scheme (14) by replacing the time step Δt with $\gamma^{-1} \Delta t$, and μ_i with $\gamma \mu_i$, because the coefficients w_{ij} will become γw_{ij} , and hence γ cancels out in both the divergence and the viscosity terms of (11). This justifies the usual approach of making μ directly and Δt inversely proportional to the size of the characteristic velocity $\mathbf{F}'(u)$.

Note that in the case of constant linear transport ($\mathbf{F}' = \text{const}$) and smooth initial condition u_0 our scheme is monotone since its weights w_{ij} only depend on the local distribution of nodes near \mathbf{x}_i , see Section 3. Hence, we may only expect convergence of first order for smooth solutions, see for example Theorem 4.12 in Hesthaven (2018), and thus the Euler method of (4) is appropriate for time discretization.

3. Minimal numerical differentiation formulas

We obtain numerical differentiation formulas (5) and (12) by minimizing certain weighted ℓ_2 -seminorms of the weight vectors $[w_{ij}]_{\mathbf{x}_j \in X_i}$ and $[v_{ij}]_{\mathbf{x}_j \in X_i}$ under equality constraints that ensure the exactness for linear, respectively, quadratic polynomials, and inequality constraints that guarantee the positivity of the scheme.

Minimization of ℓ_2 -seminorms is a standard approach in the meshless finite difference methods of polynomial type, it is equivalent to obtaining numerical differentiation formulas by applying a differential operator to a weighted least squares polynomial approximation of the data. There are many choices for the least square weights employed in the literature, see for example Jacquemin et al. (2020). We use the weights of the ℓ_2 -minimal formulas suggested in Davydov and Schaback (2018) on the basis of the error bounds of numerical differentiation. In this section we first review general notions and results related to these formulas. Subsequently, we present our approach to enforcing required properties of the weights.

Let

$$Df(\mathbf{x}) := \sum_{\alpha \in \mathbb{Z}_+^d, |\alpha| \leq k} c_\alpha(\mathbf{x}) \frac{\partial^{|\alpha|} f}{\partial x_1^{\alpha_1} \dots \partial x_d^{\alpha_d}}(\mathbf{x}) \quad (20)$$

be a linear differential operator of order k applied to a sufficiently regular function f at a point \mathbf{x} . For any $\mathbf{x} \in \bar{\Omega}$ and a set $X_{loc} \subset X$ of its neighbors in X , consider the numerical approximation

$$\hat{D}f(\mathbf{x}) := \sum_{\mathbf{x}_j \in X_{loc}} w_j f(\mathbf{x}_j) \quad (21)$$

of $Df(\mathbf{x})$ defined as a linear combination of the values of f on X_{loc} . In this paper we use two types of operators: directional derivatives $D = D_{\boldsymbol{\eta}_i}$ and the Laplace operator $D = \Delta$, and perform numerical differentiation at nodes $\mathbf{x} = \mathbf{x}_i$ on the influence sets $X_{loc} = X_i$ with weights denoted $w_j = w_{ij}$ for $D_{\boldsymbol{\eta}_i}$ and $w_j = v_{ij}$ for Δ .

If the weight vector $\mathbf{w} = [w_j]_{\mathbf{x}_j \in X_{loc}}$ is chosen such that (21) is exact for polynomials up to a certain order $q > k$,¹ then the following upper bound for the error holds (Davydov and Schaback, 2018, Theorem 7),

$$|\hat{D}f(\mathbf{x}) - Df(\mathbf{x})| \leq \sigma(\mathbf{x}, X_{loc}, \mathbf{w}) h_{\mathbf{x}, X_{loc}}^{r+\gamma-k} |f|_{r, \gamma, \Omega_{loc}}, \quad f \in C^{r, \gamma}(\Omega_{loc}), \quad k \leq r \leq q-1, \quad (22)$$

where Ω_{loc} denotes a domain containing the set $\bigcup_{\mathbf{x}_j \in X_{loc}} [\mathbf{x}, \mathbf{x}_j]$,

$$\sigma(\mathbf{x}, X_{loc}, \mathbf{w}) := h_{\mathbf{x}, X_{loc}}^{k-r-\gamma} \sum_{\mathbf{x}_j \in X_{loc}} |w_j| \|\mathbf{x}_j - \mathbf{x}\|_2^{r+\gamma}, \quad h_{\mathbf{x}, X_{loc}} := \max_{\mathbf{x}_j \in X_{loc}} \|\mathbf{x}_j - \mathbf{x}\|_2,$$

$$|f|_{r, \gamma, \Omega_{loc}} := \frac{1}{(\gamma+1) \dots (\gamma+r)} \left(\sum_{|\alpha|=r} \binom{r}{\alpha} \left| \frac{\partial^{|\alpha|} f}{\partial x_1^{\alpha_1} \dots \partial x_d^{\alpha_d}} \right|_{0, \gamma, \Omega_{loc}} \right)^{1/2}, \quad |f|_{0, \gamma, \Omega_{loc}} := \sup_{\substack{\mathbf{x}, \mathbf{y} \in \Omega_{loc} \\ \mathbf{x} \neq \mathbf{y}}} \frac{|f(\mathbf{x}) - f(\mathbf{y})|}{\|\mathbf{x} - \mathbf{y}\|_2^\gamma},$$

and $C^{r, \gamma}(\Omega_{loc})$, $r \geq 0$, $\gamma \in (0, 1]$, denotes the space consisting of all r times continuously differentiable functions f on Ω_{loc} such that $|f|_{r, \gamma, \Omega_{loc}} < \infty$. Note that the value of $\sigma(\mathbf{x}, X_{loc}, \mathbf{w})$ does not depend on the size $h_{\mathbf{x}, X_{loc}}$ of the neighborhood of \mathbf{x} , but only on the cardinality and the shape of X_{loc} , as well as on the choice of the weights. Therefore the convergence order of the approximation as $h_{\mathbf{x}, X_{loc}} \rightarrow 0$ is determined by the power of $h_{\mathbf{x}, X_{loc}}$ in (22) unless the sets X_{loc} are in specific bad positions (for example, contained in zero sets of some polynomials of order q), that normally do not realize on irregular nodes.

As long as the exactness for polynomials of order up to $q > k$ does not determine the weights w_j uniquely, in particular when the number n_{loc} of nodes in X_{loc} is greater than $\dim \Pi_q^d = \binom{d+q-1}{d}$, different strategies for a suitable selection of the weights can be considered. The obvious choice of minimizing $\sigma(\mathbf{x}, X_{loc}, \mathbf{w})$ leads to the ℓ_1 -minimal formulas that can be computed by linear programming. A computationally more attractive alternative is to minimize the weighted ℓ_2 -seminorm

$$|\mathbf{w}|_{2, r+\gamma} := \left(\sum_{\mathbf{x}_j \in X_{loc}} w_j^2 \|\mathbf{x}_j - \mathbf{x}\|_2^{2(r+\gamma)} \right)^{1/2}, \quad (23)$$

which leads to the ℓ_2 -minimal formula (21) satisfying

$$|\hat{D}f(\mathbf{x}) - Df(\mathbf{x})| \leq \sqrt{n_{loc}} \rho(\mathbf{x}, X_{loc}) h_{\mathbf{x}, X_{loc}}^{r+\gamma-k} |f|_{r, \gamma, \Omega_{loc}}, \quad f \in C^{r, \gamma}(\Omega_{loc}), \quad k \leq r \leq q-1, \quad (24)$$

where

$$\rho(\mathbf{x}, X_{loc}) := \inf \left\{ \sigma(\mathbf{x}, X_{loc}, \mathbf{w}) : \mathbf{w} \in \mathbb{R}^{n_{loc}}, Dp(\mathbf{x}) = \sum_{\mathbf{x}_j \in X_{loc}} w_j p(\mathbf{x}_j) \text{ for all } p \in \Pi_q^d \right\}.$$

Despite the additional factor $\sqrt{n_{loc}}$ in (24) in comparison to the ℓ_1 -minimal formulas, both types of formulas behave similarly in numerical experiments, see further details in Davydov and Schaback (2018).

¹The existence of the solution obtained by imposition of the exactness conditions, which may not be achieved for some special geometry of the set X_{loc} , is guaranteed for example if X_{loc} is unisolvent for the polynomial space of interest.

Inequality constrained minimal formulas

In the case of Laplace operator $\Delta f = \frac{\partial^2}{\partial x_1^2} + \dots + \frac{\partial^2}{\partial x_d^2}$ it is often attractive to enforce the *positivity* of the weight vector \mathbf{w} in (21), by requiring that $\mathbf{x} \in X_{loc}$ and $w_j \geq 0$ for all $\mathbf{x}_j \in X_{loc} \setminus \{\mathbf{x}\}$. (Then $w_j < 0$ for $\mathbf{x}_j = \mathbf{x}$ because of the exactness for constant.) This for example helps to ensure that system matrices of the resulting meshless finite difference method for the Poisson equation are M-matrices, with various benefits for the numerical solution, see Seibold (2008) and references therein. In (Davydov and Schaback, 2018, Section 4.3) an error bound is obtained for positive formulas for elliptic differential operators of second order.

We generate inequality constrained ℓ_2 -minimal formulas in the form (5) and (12) for the operators $D_{\eta_i}(\mathbf{x}_i)$ and $\Delta_{\mathbf{x}}(\mathbf{x}_i)$ that minimize (23) with parameters r, γ chosen to take into account the error bound (22) as follows. The algorithm depends on the prescribed bounds n_{\min}, n_{\max} for the size of the set of influence and the artificial viscosity parameter $\mu_i \geq 0$. We start by choosing an initial set of influence $X_i = X_i^{init}$ consisting of $|X_i^{init}| = n_{\min}$ nearest neighbors of \mathbf{x}_i in X , including \mathbf{x}_i itself. (We use $n_{\min} = 10$ in the numerical experiments in the bivariate case $d = 2$.)

If $\mu_i > 0$, then we first compute the weight vector $\mathbf{v}_i = [v_{ij}]_{\mathbf{x}_j \in X_i}$, $X_i = X_i^{visc}$, as the solution of the quadratic minimization problem

$$\min_{\mathbf{v}} |\mathbf{v}|_{2,3}^2 \quad \text{subject to (13) and the inequalities } v_{ij} \geq 0 \quad \forall \mathbf{x}_j \in X_i \setminus \{\mathbf{x}_i\}, \quad (25)$$

where

$$|\mathbf{v}|_{2,3} = \left(\sum_{\mathbf{x}_j \in X_i} v_{ij}^2 \|\mathbf{x}_j - \mathbf{x}_i\|_2^6 \right)^{1/2},$$

which corresponds to the case $q = 3, r = 2, \gamma = 1$ of the ℓ_2 -minimal formulas, and $X_i = X_i^{visc}$ is either X_i^{init} , or a larger set obtained by repeatedly expanding X_i to the set of $\lceil 1.2|X_i| \rceil$ nearest neighbors of \mathbf{x}_i should (25) be infeasible. In order to avoid an infinite loop we terminate the process if the new size is greater than n_{\max} , in which case we refrain from using artificial viscosity for the node \mathbf{x}_i and set $\mu_i = 0$. In our bivariate experiments with $n_{\max} = 100$ this never happened for interior nodes \mathbf{x}_i . Since (25) is often infeasible for boundary nodes even for a large X_i , we set $\mu_i = 0$ whenever $\mathbf{x}_i \in \partial\Omega$.

After \mathbf{v}_i is chosen as explained above (or set formally to zero if $\mu_i = 0$), we compute the weight vector $\mathbf{w}_i = [w_{ij}]_{\mathbf{x}_j \in X_i}$ as the solution of the quadratic minimization problem

$$\min_{\mathbf{w}} |\mathbf{w}|_{2,2}^2 \quad \text{subject to (10) and the inequalities } w_{ii} \leq B, w_{ij} \leq 0 \quad \forall \mathbf{x}_j \in X_i \setminus \{\mathbf{x}_i\}, \quad (26)$$

where

$$|\mathbf{w}|_{2,2} = \left(\sum_{\mathbf{x}_j \in X_i} w_{ij}^2 \|\mathbf{x}_j - \mathbf{x}_i\|_2^4 \right)^{1/2},$$

which corresponds to the case $q = 2, r = 1, \gamma = 1$ of the ℓ_2 -minimal formulas, the constant B is given by

$$B = \max \left\{ \frac{1}{2\Delta t}, \frac{1}{\Delta t} - \mu_i |v_{ii}| \right\} \quad (27)$$

and X_i is initialized as X_i^{init} if $\mu_i = 0$ or X_i^{visc} otherwise, and repeatedly expanded to the set of $\lceil 1.2|X_i| \rceil$ nearest neighbors of \mathbf{x}_i as long as (26) is infeasible. Note that v_{ii} is negative as soon as $\mu_i > 0$ because of (17) and since v_{ij} , $\mathbf{x}_j \in X_i$, cannot all be zero thanks to (13). Again, we terminate the process if the new size is greater than n_{\max} , meaning the algorithm exits with failure. In this case we repeat the same procedure as above after removing the inequality constraints in (26) and resetting X_i to X_i^{init} if $\mu_i = 0$ or X_i^{visc} otherwise. With $n_{\max} = 100$ in the bivariate case this happened very rarely and only for certain interior nodes situated very close to the inflow boundary nodes in Example 1 below, see Section 6.1. We set $v_{ij} = 0$ for all j such that $\mathbf{x}_j \in X_i \setminus X_i^{visc}$. Note that the largest size of X_i observed in the numerical experiments of Section 6 was 27 for both the viscosity term (X_i^{visc}) and the divergence term (final X_i) when using the nodes of the Cartesian grid or Halton points, and reaching at most 40 for the viscosity term and 48 for the divergence term in the case of random nodes of Example 2 in Section 6.2.

Finally, we correct μ_i if needed, by setting

$$\mu_i = \min \left\{ \mu_i, \frac{1}{2\Delta t |v_{ii}|} \right\}. \quad (28)$$

It is easy to check that the resulting weights satisfy the positivity conditions (15) and (16) with updated μ_i .

Clearly, the algorithm described here is not the only possible scenario to ensure the positivity of the scheme. Minimization of $|\mathbf{v}|_{2,3}$ and $|\mathbf{w}|_{2,2}$ is motivated by the error bound (24). The weights v_{ij} are computed before w_{ij} because after knowing v_{ii} we often obtain via (27) a weaker constraint $w_{ii} \leq B$ in (26), which may help to somewhat reduce the size of X_i and hence reduce the factor $\sigma(\mathbf{z}, X_{\mathbf{z}}, \mathbf{w})$ in (22), improving the accuracy of the numerical differentiation. Different approaches to computing v_{ij} , w_{ij} and organizing their interaction and adjustment of μ_i are possible and should be explored in the future. The version presented here works well in the numerical experiments presented in Section 6.

Remark 1. Note that the positivity of the scheme may be enforced via the choice of the positive artificial viscosity weight vector \mathbf{v} and the coefficient $\mu_i > 0$, which would allow the weight vectors \mathbf{w} for the directional derivatives to fail the condition $w_{ij} \leq 0$, $j \neq i$. However, this would mean that we have to apply stronger inequality constraints on \mathbf{v} in the form $\mu_i v_{ij} \geq w_{ij}$ whenever $w_{ij} > 0$ (assuming \mathbf{w} is computed before \mathbf{v}). In particular, we would not be able to choose $\mu_i = 0$, which would rule out adaptive viscosity as in Algorithm 3 below, where μ_i vanishes at some distance from the faults in the solution. Moreover, a sufficiently large $\mu_i > 0$ may be needed in this case, increasing the numerical dissipation unnecessarily. In contrast to this, our approach allows to add just enough artificial viscosity to ensure shock capturing, without burdening it by a second task of stabilizing the scheme.

4. Adaptive fault-based viscosity

Since the stability of our scheme is guaranteed by its positivity, the artificial viscosity term is only responsible for the correct resolution of shocks. Therefore it is desirable to choose the viscosity parameter μ_i in (14) adaptively, in particular setting it to zero for nodes \mathbf{x}_i that are far from the shock front, which improves the local accuracy of the overall scheme because local numerical differentiation weights \tilde{w}_{ij} in this case coincide with the weights w_{ij} of the unconstrained ℓ_2 -minimal formula, in contrast to the combined weights $\tilde{w}_{ij} = w_{ij} - \mu_i v_{ij}$ when $\mu_i > 0$, that lose the ℓ_2 -minimality. Since the solution u exhibits jump discontinuities at the shock fronts, we choose $\mu_i > 0$ only for nodes that are close to the discontinuities of the discrete numerical solution $U(t, \mathbf{x}_j)$, $j = 1, \dots, N$, of the previous time step, identified by a fault detection method. We refer to Guermond and Popov (2017) and references therein for algorithms relying on adaptive viscosity in the context of the finite element and finite volume methods for conservation laws.

We make use of the fault indicator introduced in Bracco et al. (2019) that also relies on the minimal differentiation formulas described in Section 3. Given a set of scattered nodes $X \subset \mathbb{R}^d$, with associated function values $f(\mathbf{x})$, $\mathbf{x} \in X$, it allows us to determine which nodes are close to a discontinuity of f . In many applications discontinuities form curves, which are referred to as *faults* in the literature.

For each $\mathbf{x}_i \in X$, let $X_{i,\mathcal{F}} \subseteq X$ be the set of $n_{\mathcal{F}}$ points $\mathbf{x}_j \in X$ closest to \mathbf{x}_i . We define the *fault indicator*

$$I_{\Delta}(\mathbf{x}_i, n_{\mathcal{F}}) := \frac{|\hat{\Delta}f(\mathbf{x}_i)|}{\sum_{\mathbf{x}_j \in X_{i,\mathcal{F}}} |w_j| \|\mathbf{x}_j - \mathbf{x}_i\|_2^2}, \quad (29)$$

where

$$\hat{\Delta}f(\mathbf{z}) := \sum_{\mathbf{x}_j \in X_{i,\mathcal{F}}} w_j f(\mathbf{x}_j) \quad (30)$$

is the ℓ_2 -minimal differentiation formula approximating the Laplacian $\Delta f(\mathbf{x}_i)$ with polynomial exactness order $q = 3$ and minimizing the seminorm $|\mathbf{w}|_{2,3}$. Note that the second fault indicator introduced in Bracco et al. (2019), employing the gradient instead of the Laplace operator, can also be used and gives comparable results in numerical experiments. We opted for the Laplacian-based one because it is cheaper. Indeed,

the approximation of the scalar-valued Laplace operator by a numerical differentiation formula requires significantly less computational effort than approximating the vector-valued gradient operator.

In Bracco et al. (2019) we have shown (see Theorem 2 there) the following property of the indicator (29),

$$I_{\Delta}(\mathbf{x}_i, n_{\mathcal{F}}) \leq |f|_{1,1,\Omega_{loc}}, \quad (31)$$

with Ω_{loc} as in (22). Although (31) is stated in Bracco et al. (2019) only for the bivariate case, it is easy to extend it to any number of variables d . Indeed, this follows from the fact that Theorem 3 in Bracco et al. (2019) holds for any d with the same proof. It is remarkable that the estimate (31) does not contain any unknown constants and therefore allows for comparison between different \mathbf{x}_i independently of how irregular each local node set $X_{i,\mathcal{F}}$ is. Therefore, a large value of $I_{\Delta}(\mathbf{x}_i, n_{\mathcal{F}})$ indicates that f is likely to be discontinuous in Ω_{loc} , or at least its gradient tends to change abruptly there, that is the behavior expected from the solution of a conservation law in the vicinity of a shock front. Moreover, it is shown in the bivariate case in Theorem 6 of Bracco et al. (2019) that $I_{\Delta}(\mathbf{x}_i, n_{\mathcal{F}})$ behaves like $O(h^{-2})$ as \mathbf{x}_i approaches a fault and $\text{diam}(X_{i,\mathcal{F}}) \rightarrow 0$, while it is bounded if \mathbf{x}_i stays sufficiently far from all faults. In other words, the indicator tends to take large values at points close to faults and bounded values at points far from them, which justifies classifying as close to a fault the points of the set

$$\mathcal{F}(\alpha, X) := \{\mathbf{x}_i \in X : I_{\Delta}(\mathbf{x}_i, n_{\mathcal{F}}) > \alpha\},$$

with $\alpha > 0$ being a suitable threshold.

Thanks to these properties of the indicator, a reasonable choice of α is the median value of I_{Δ} computed on the nodes in X . This works well, except when f is constant or linear in large subareas of the domain, since $\Delta f(\mathbf{z}) = 0$ and so $I_{\Delta}(\mathbf{x}_i, n_{\mathcal{F}}) \approx 0$ for any \mathbf{x}_i belonging to these areas, and α , chosen as the median value, would be very close to 0. As a result, all the points where the value of the indicator is slightly above 0 would be marked as close to a fault even if they are not. For this reason, we use the following two-step fault detection algorithm, that has shown excellent performance in extensive numerical tests on scattered data presented in Bracco et al. (2019).

Computation of the set of fault nodes $\mathcal{F}(X)$.

- Set $\alpha_1 = C_1 \text{median}\{I_{\Delta}(\mathbf{x}_i, n_{\mathcal{F}}) : \mathbf{x}_i \in X\}$, and compute $\mathcal{F}(\alpha_1, X)$.
- Set $\alpha_2 = C_2 \text{median}\{I_{\Delta}(\mathbf{x}_i, n_{\mathcal{F}}) : \mathbf{x}_i \in \mathcal{F}(\alpha_1, X)\}$, and compute the final set of fault nodes as $\mathcal{F}(X) := \mathcal{F}(\alpha_2, \mathcal{F}(\alpha_1, X))$.

Note that in all numerical experiments of Section 6 we use $C_1 = 1$ and $C_2 = 2$, the same values that proved to be effective in the experiments of Bracco et al. (2019), as our goal is to provide a robust choice, avoiding a fine-tuning of the parameters example by example.

Adaptive artificial viscosity

We now describe our approach to choosing the factor μ_i in (14) when adaptive fault-based viscosity is used. As input we need the set of nodes X , the values $U(t, \mathbf{x}_i)$ for all $\mathbf{x}_i \in X$, and the *spacing* h for the node set X . Spacing h is a parameter that we use in the node generation as explained in Section 6, with $h \approx (|\Omega|/N)^{1/d}$. In addition we need three user specified parameters: μ , the maximum factor for the artificial viscosity terms; the number $n_{\mathcal{F}}$ of nearest nodes for the computation of the fault indicator, which we choose to be the same number $n_{\mathcal{F}} = n_{\min}$ as in Section 3; and the constant C_3 that governs the transition zone between $\mu_i > 0$ and $\mu_i = 0$ in order to avoid abrupt changes in μ_i , that otherwise have an adverse effect on the performance of the method. Note that the advantages of a continuous transition of the amount of the artificial viscosity between zero in the regions where the solution is smooth and its maximum value where the solution is discontinuous have been observed for other numerical methods, see for example Section 12.2.3 in Hesthaven (2018). We use $C_3 = 5$ in the experiments of Section 6.

Local viscosity parameter μ_i .

- For each $\mathbf{x}_i \in X$, choose the set $X_{i,\mathcal{F}} = X_i^{init}$ consisting of $n_{\mathcal{F}}$ nearest neighbors of \mathbf{x}_i in X , and compute $\mathcal{F}(X) \subset X$ according to the above fault detection algorithm, with f on X given by $f(\mathbf{x}_j) = U(t, \mathbf{x}_j)$, $j = 1, \dots, N$.
- For each $\mathbf{x}_i \in X$, find the distance ρ_i to the set $\mathcal{F}(X)$, $\rho_i := \min \{\|\mathbf{x}_i - \mathbf{x}_j\|_2 : \mathbf{x}_j \in \mathcal{F}(X)\}$, and set

$$\mu_i = \max \left\{ 0, 1 - \frac{\rho_i}{C_3 h} \right\} \mu. \quad (32)$$

In particular, $\mu_i = 0$ as long as $\rho_i \geq C_3 h$.

Fault points and the values of μ_i are illustrated in Figure 6.8 in the numerical examples section of the paper.

5. Summary of algorithms

We now describe three versions of the positive schemes for (3), differing in their approaches to the artificial viscosity. All three algorithms rely on the following input data, while artificial viscosity requires further setup parameters detailed for Algorithms 2 and 3 that make use of it.

Input:

- Data of the problem: derivative of the flux \mathbf{F}' , domain $\Omega \subseteq \mathbb{R}^d$, the function u_0 that defines the initial condition (2), final time T , data for the boundary conditions whenever appropriate.
- Parameters of the numerical scheme: discretization nodes X , step-size in time $\Delta t > 0$, minimum and maximum number of closest neighbors n_{\min} and n_{\max} for the sets of influence.

The **output** of each scheme is the set of values

$$U(k\Delta t, \mathbf{x}_i), \quad i = 1, \dots, N, \quad \text{and } k \in \mathbb{N} \text{ with } k\Delta t \leq T,$$

as approximations of $u(k\Delta t, \mathbf{x}_i)$, for the solution u of the conservation law (1).

Our first algorithm does not add any artificial viscosity, which is appropriate when the shocks are absent.

Algorithm 1. Positive scheme without artificial viscosity.

- Initialization: Set $t = 0$ and $U(0, \mathbf{x}_i) = u(0, \mathbf{x}_i)$, $i = 1, \dots, N$.
- While $t + \Delta t \leq T$:
 - For each \mathbf{x}_i , $i = 1, \dots, N$:
 1. Compute the set of influence X_i and the weights w_{ij} , $j \in X_i$, of an inequality constrained minimal formula, as described in Section 3, with $\mu_i = 0$.
 2. Compute $U(t + \Delta t, \mathbf{x}_i)$ by (4).
 - Set $t := t + \Delta t$.

As mentioned above, adding small artificial viscosity is motivated by the principle of vanishing viscosity, and its goal is to allow accurate computation of the solution in the presence of shocks. As a side effect, solutions computed with artificial viscosity are smoother, which is normally not desired, but sometimes also produces better shapes by reducing non-physical behavior of the numerical solution near discontinuities. This latter positive effect is not significant for our method because consistent positive schemes satisfy the local maximum principle (9) and therefore do not suffer from artificial oscillations.

Algorithm 2. Positive scheme with constant artificial viscosity.

- Additional input parameter: viscosity factor $\mu > 0$.

- Initialization: Set $t = 0$ and $U(0, \mathbf{x}_i) = u(0, \mathbf{x}_i)$, $i = 1, \dots, N$.
- While $t + \Delta t \leq T$:
 - For each \mathbf{x}_i , $i = 1, \dots, N$:
 1. Compute the set of influence X_i and the weights v_{ij} and w_{ij} , $j \in X_i$, of the inequality constrained minimal formulas, as described in Section 3, with $\mu_i = \mu$.
 2. Compute $U(t + \Delta t, \mathbf{x}_i)$ by (14) with $\mu_i = \mu$.
 - Set $t := t + \Delta t$.

Finally, we consider a scheme where viscosity is only added for points that are close to discontinuities (faults) detected by the method described in Section 4. The goal is to improve approximation quality in the smooth regions because the resulting discretization of $D_{\mathbf{n}_i}$ in (5) will allow a smaller set of influence X_i and smaller seminorm $|\mathbf{w}_i|_{2,2}$ of the weight vector $\mathbf{w}_i = [w_{ij}]_{\mathbf{x}_j \in X_i}$ minimized in (26), in comparison to the weights $\tilde{w}_{ij} = w_{ij} - \mu_i v_{ij}$ effectively used in (14) when $\mu_i > 0$. In addition, this scheme avoids the computation of the positive weights for the approximation of the Laplacian in most of the domain, leading to a significant computational saving. In fact, the computation of the approximation of the Laplacian involved in the expression of the fault indicator (29) is less expensive since a minimal differentiation formula without sign constraints on the weights is employed, without an adaptive expansion of the influence set needed for the inequality constrained weights.

Algorithm 3. Positive scheme with adaptive fault-based artificial viscosity.

- Additional input parameters: maximum viscosity factor $\mu > 0$, spacing h of the node set X , fault detection parameters $n_{\mathcal{F}}, C_1, C_2$ and transition zone parameter C_3 .
- Initialization: Set $t = 0$ and $U(0, \mathbf{x}_i) = u(0, \mathbf{x}_i)$, $i = 1, \dots, N$.
- While $t + \Delta t \leq T$:
 - Apply the fault detection method presented in Section 4 to the point set X and the corresponding solution values $\{U(t, \mathbf{x}), \mathbf{x} \in X\}$ with parameters $n_{\mathcal{F}}, C_1, C_2$, obtaining the set of fault nodes $\mathcal{F}(X) \subset X$.
 - For each \mathbf{x}_i , $i = 1, \dots, N$:
 1. Compute the individual viscosity factor μ_i by (32), using $\mathcal{F}(X)$, μ , h and C_3 as described in Section 4.
 2. Compute the set of influence X_i and the weights v_{ij} and w_{ij} , $j \in X_i$, of the inequality constrained minimal formulas, as described in Section 3.
 3. Compute $U(t + \Delta t, \mathbf{x}_i)$ by (14).
 - Set $t := t + \Delta t$.

6. Numerical examples

In this section we report numerical results obtained by applying our positive schemes to three bivariate benchmark problems selected to highlight different aspects of the method.

In order to test our method on irregular nodes we initialize X as a set of M quasi-random Halton points in a square $\Omega \subset \mathbb{R}^2$, where M is determined by the *spacing* parameter $h > 0$ and side length ℓ of the square by rounding $(\ell/h)^2$ to the nearest integer. Then all nodes with distance to the boundary of Ω at most $0.25h$ are removed from X . Although Halton points already provide a good representative of irregularities expected in meshless node generation, see Suchde et al. (2022), in Example 2 we also test the performance of our method on the more severe random points obtained in a similar manner by MATLAB's pseudo-random number generator. In the case of periodic boundary conditions (Examples 2 and 3) we extend X periodically

to a larger domain, which simplifies the computation of the sets of influence. Example 1 requires additional nodes on the boundary, as explained in Section 6.1. Whenever we use a Cartesian grid, h is the usual step size. Therefore the same spacing h corresponds to comparable numbers N of nodes for the grids and Halton points.

The parameters of our schemes are chosen in a unified way in all examples. In particular, we make the viscosity factor μ directly and the time step Δt inversely proportional to the maximum size of the characteristic velocity $\mathbf{F}'(u_0)$ by setting $\mu = 0.5h v_0$ and $\Delta t = 0.2h/v_0$, where $v_0 := \max_{\mathbf{x} \in \bar{\Omega}} \|\mathbf{F}'(u_0)\|_\infty$. We always take $n_{\min} = 10$, $n_{\max} = 100$, $\Delta t = 0.2h$ and choose the final time T such that $K = T/\Delta t$ is an integer. The viscosity or maximum viscosity factor is always $\mu = 0.5h$, and additional parameters of the fault-based viscosity are chosen as $n_{\mathcal{F}} = 10$, $C_1 = 1$, $C_2 = 2$, $C_3 = 5$.

In addition to the qualitative assessment of the results by comparing 3D plots of the solutions, we also compute the error measures

$$E_1 = \frac{1}{N} \sum_{i=1}^N |U(T, \mathbf{x}_i) - U_{\text{ref}}(T, \mathbf{x}_i)|, \quad \text{and} \quad E_2 = \left(\frac{1}{N} \sum_{i=1}^N (U(T, \mathbf{x}_i) - U_{\text{ref}}(T, \mathbf{x}_i))^2 \right)^{1/2}$$

with respect to a reference solution U_{ref} given either by an exact solution (available in Example 1), or by a high resolution solution, obtained on a dense Cartesian grid with an appropriate higher order method provided in the code supplement of the book [Hesthaven \(2018\)](#). In the case of an irregular set X , the values $U_{\text{ref}}(T, \mathbf{x}_i)$ are obtained by piecewise linear interpolation of $U_{\text{ref}}(T, \cdot)$ on the Delaunay triangulation of the Cartesian grid. Note that E_1 and E_2 may be considered as discrete replacements for the L^1 and L^2 errors on Ω , respectively.

6.1. Example 1: Inviscid Burgers' equation with discontinuous initial condition

In the first example we consider the inviscid Burgers' equation with flux $\mathbf{F}(u) = \frac{1}{2}u^2\mathbf{v}$, $\mathbf{v} = (1, 1)$ on the spatial domain $\Omega = [0, 1]^2$, with discontinuous initial condition

$$u_0(\mathbf{x}) = u_0(x, y) = \begin{cases} -0.2 & \text{if } x < 0.5 \text{ and } y > 0.5, \\ -1 & \text{if } x > 0.5 \text{ and } y > 0.5, \\ 0.5 & \text{if } x < 0.5 \text{ and } y < 0.5, \\ 0.8 & \text{if } x > 0.5 \text{ and } y < 0.5, \end{cases}$$

and exact solution given for $t > 0$ by

$$u(\mathbf{x}) = u(x, y) = \begin{cases} -0.2 & \text{if } x < \frac{1}{2} - \frac{3t}{5} \text{ and } y > \frac{1}{2} + \frac{3t}{20}, \\ 0.5 & \text{if } x < \frac{1}{2} - \frac{3t}{5} \text{ and } y < \frac{1}{2} + \frac{3t}{20}, \\ -1 & \text{if } \frac{1}{2} - \frac{3t}{5} < x < \frac{1}{2} - \frac{t}{4} \text{ and } y > \frac{-8x}{7} + \frac{15}{4} - \frac{15t}{28}, \\ 0.5 & \text{if } \frac{1}{2} - \frac{3t}{5} < x < \frac{1}{2} - \frac{t}{4} \text{ and } y < \frac{-8x}{7} + \frac{15}{4} - \frac{15t}{28}, \\ -1 & \text{if } \frac{1}{2} - \frac{t}{4} < x < \frac{1}{2} + \frac{t}{2} \text{ and } y > \frac{x}{6} + \frac{5}{12} - \frac{5t}{24}, \\ 0.5 & \text{if } \frac{1}{2} - \frac{t}{4} < x < \frac{1}{2} + \frac{t}{2} \text{ and } y < \frac{x}{6} + \frac{5}{12} - \frac{5t}{24}, \\ -1 & \text{if } \frac{1}{2} + \frac{t}{2} < x < \frac{1}{2} + \frac{4t}{5} \text{ and } y > x - \frac{5}{18t}(x + t - \frac{1}{2})^2, \\ \frac{2x-1}{2t} & \text{if } \frac{1}{2} + \frac{t}{2} < x < \frac{1}{2} + \frac{4t}{5} \text{ and } y < x - \frac{5}{18t}(x + t - \frac{1}{2})^2, \\ -1 & \text{if } x > \frac{1}{2} + \frac{4t}{5} \text{ and } y > \frac{1}{2} - \frac{t}{10}, \\ 0.8 & \text{if } x > \frac{1}{2} + \frac{4t}{5} \text{ and } y < \frac{1}{2} - \frac{t}{10}, \end{cases}$$

see [Guermond et al. \(2011\)](#). Inflow boundary conditions are derived from the above formula for the exact solution. The solution at time $T = 0.5$ is presented in Figure 6.1(a).

We choose spacing $h = 0.01$ and generate $10000 = 1/h^2$ Halton points in the unit square, from which we remove all points with distance less than $0.25h$ from the boundary, while we add the points obtained by

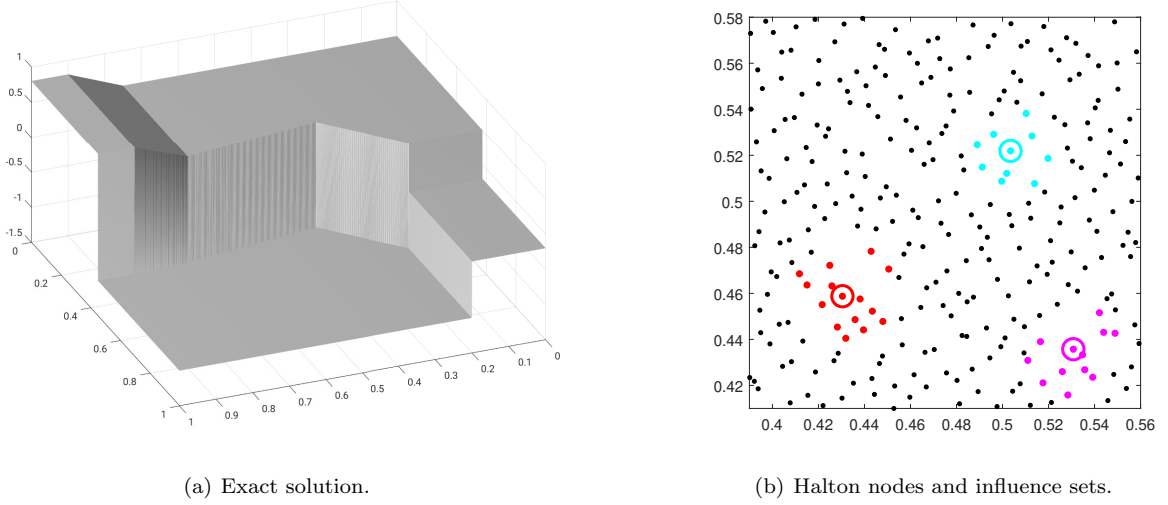
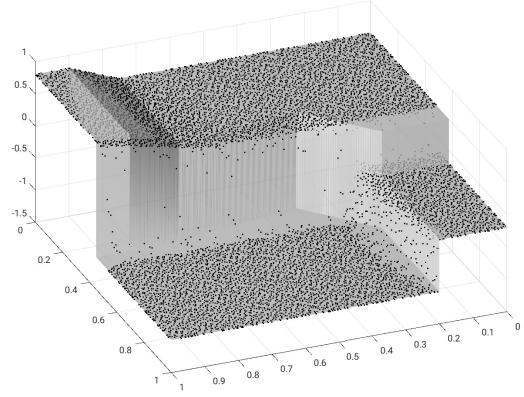
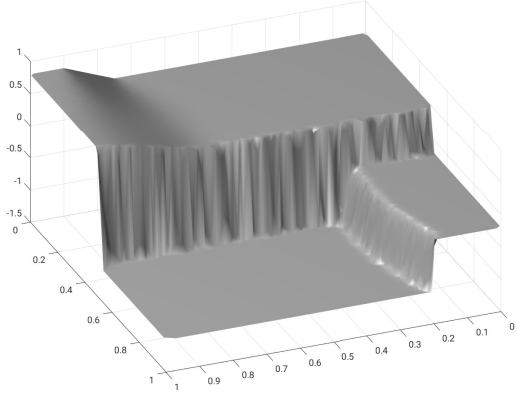


Figure 6.1: Example 1: Exact solution and a zoom of the node set, with three highlighted influence sets X_i (the encircled point is \mathbf{x}_i) of size 10 (in cyan), 12 (in magenta), and 15 (in red).

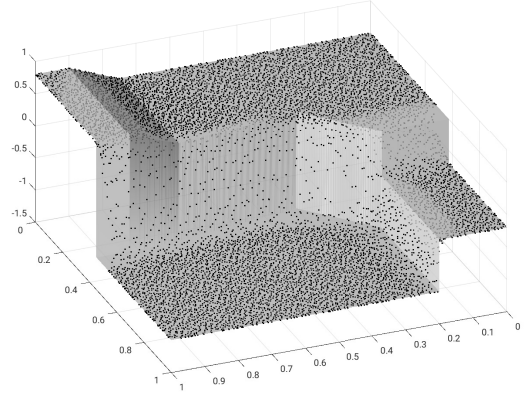
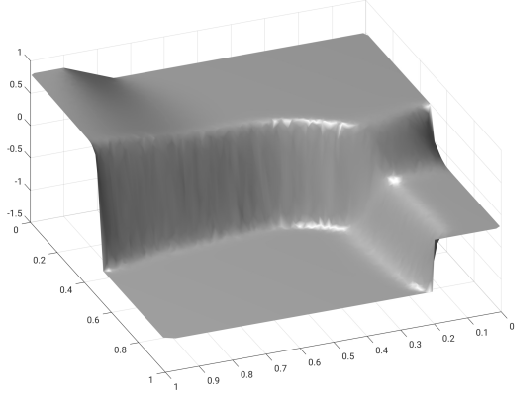
projecting to the boundary the Halton points at distance less than h from it. This makes a rather irregular distribution of the boundary nodes, as seen in the right plots of Figure 6.2.

At each time step we identify inflow boundary nodes as those $\mathbf{x}_i \in X \cap \partial\Omega$, for which the approximated flow direction $\boldsymbol{\eta}_i = \mathbf{F}'(U(t, \mathbf{x}_i))$ points inside Ω . For these nodes, we set $U(t + \Delta t, \mathbf{x}_i) := u(t + \Delta t, \mathbf{x}_i)$ according to the above formula for the exact solution. For all other boundary and interior nodes the value $U(t + \Delta t, \mathbf{x}_i)$ is computed according to the respective algorithm of Section 5 in use. Since the minimization problem (25) turns out to be infeasible even with $n_{\max} = 100$ neighbors for many boundary nodes, we always set $\mu_i = 0$ if $\mathbf{x}_i \in \partial\Omega$ in order to switch off the artificial viscosity for these nodes. For certain nodes (fewer than 20) situated in the immediate neighborhood of the inflow boundary, the minimization problem (26) is infeasible, and we use minimal numerical differentiation without inequality constraints to compute the weights w_{ij} . This does not generate instability in our experiments. In Figure 6.1(b) we show three examples of employed influence sets.

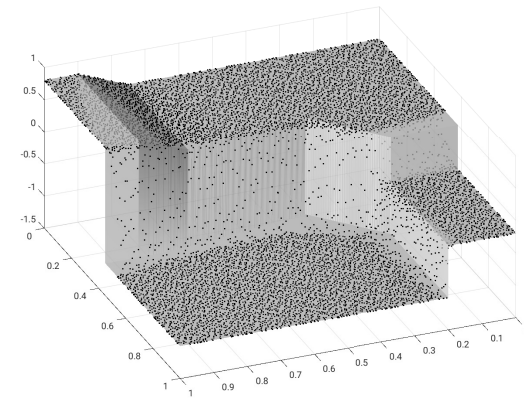
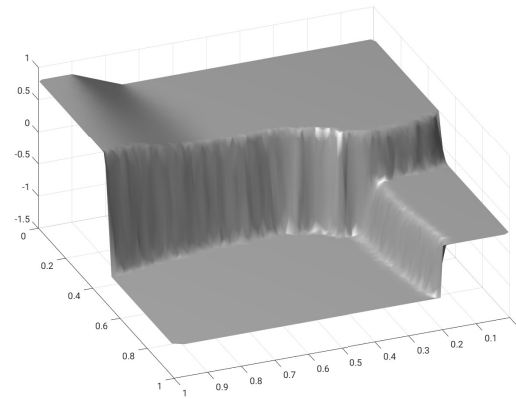
Numerical solutions at time $T = 0.5$ obtained by Algorithms 1–3 are presented in Figures 6.2 and 6.3. Here, Figure 6.2 gives 3D visualizations of the discrete solutions on the left and point cloud-based scatter plots over a transparent exact solution on the right, and Figure 6.3 provides the view from above, with the plot in 6.3(a) based on the exact solution on the same Halton nodes as in Figure 6.2. Note that the wrinkles near discontinuities in the left plots of Figures 6.2 are visualization artefacts, whereas the actual solutions are discrete as shown on the right. We observe that there are no instabilities in either solution, which is justified by the maximum principle (9) guaranteed for any positive scheme. However, the positive scheme without viscosity (Algorithm 1) completely misses an essential feature of the solution by straightening out one of discontinuity curves, which confirms that the stability and consistency of the scheme on their own do not guarantee a physically correct approximation when shocks are present. The shapes are much closer to the exact solution for Algorithms 2 and 3, indicating that the artificial viscosity gives a crucial contribution to the accuracy of the method. Moreover, the comparison between the solutions obtained by the positive scheme with constant and adaptive viscosity, see (c) and (d) in both Figures 6.2 and 6.3, reveals that the adaptive method significantly improves the solution in the crucial areas near discontinuities that look much sharper in the plots. In addition we provide errors E_1 and E_2 for the three solutions in Table 6.1. While they are significantly higher for Algorithm 1, there is little difference between Algorithms 2 and 3. However, this quantitative comparison is somewhat misleading as it is slightly in favor of Algorithm 2, in contrast to the clear visual evidence giving a significant advantage to Algorithm 3.



(a) No viscosity (Algorithm 1).



(b) Constant viscosity (Algorithm 2).



(c) Adaptive viscosity (Algorithm 3).

Figure 6.2: Example 1: Visual comparison of numerical solutions for $T = 0.5$. For each algorithm, the 3D visualization of the discrete solution (left) is shown together with the point cloud-based scatter plot over a transparent exact solution (right).

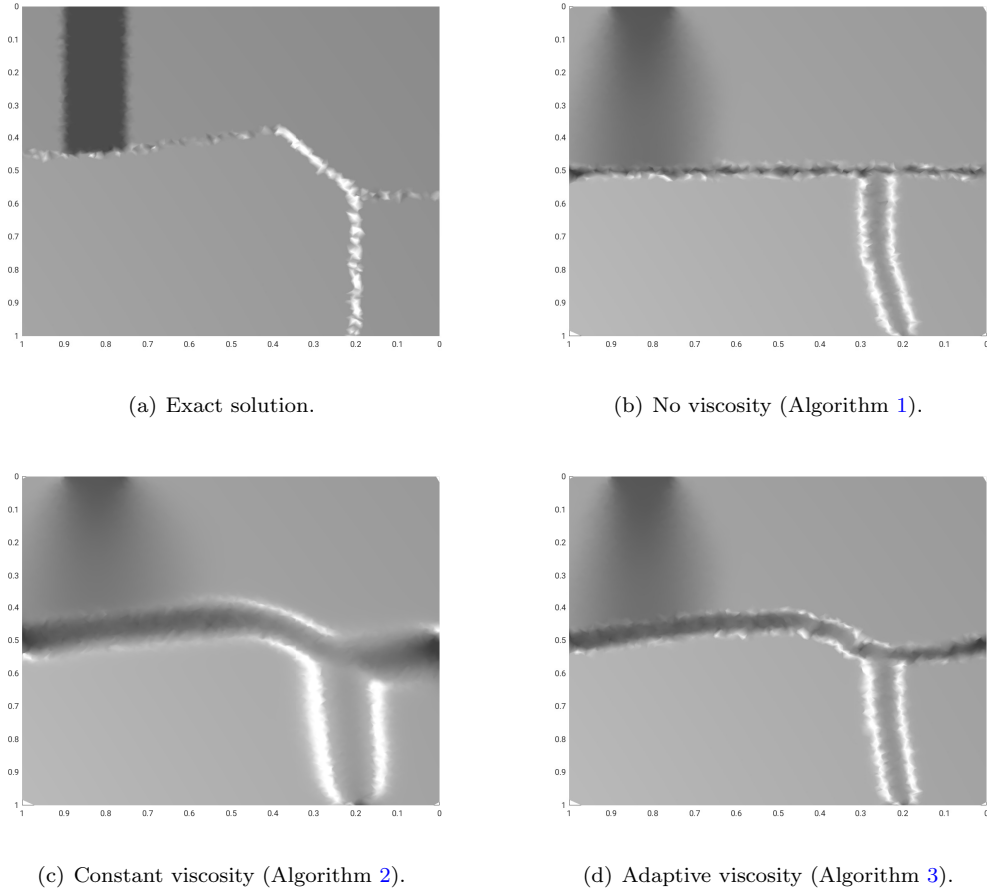


Figure 6.3: Example 1: Visual comparison of numerical solutions for $T = 0.5$: view from above.

method	E_1 -error	E_2 -error
no viscosity (Algorithm 1)	1.18e-01	3.89e-01
constant viscosity (Algorithm 2)	6.43e-02	2.38e-01
adaptive viscosity (Algorithm 3)	7.04e-02	2.78e-01

Table 6.1: Example 1: Errors of solutions for $T = 0.5$ obtained by Algorithms 1–3.

Note that our solutions are less accurate than those presented in [Guermond et al. \(2011\)](#) for comparable node spacing, which is expectable since our methods are of first order, in contrast to the higher order methods employed in that paper.

6.2. Example 2: Inviscid Burgers' equation with smooth initial condition

In the second example we again consider inviscid Burgers' equation with the flux $\mathbf{F}(u) = \frac{1}{2}u^2\mathbf{v}$, $\mathbf{v} = (1, 1)$, this time with periodic boundary conditions on the spatial domain $\Omega = [0, 0.5]^2$, and with the smooth initial condition

$$u_0(\mathbf{x}) = \sin(8\pi(x_1 + x_2/2)).$$

In spite of the initial condition being smooth, a shock appears as time advances. Note that this problem is an adaptation of the example given in Section 7.1.1 of [Hesthaven \(2018\)](#), where the flux is chosen slightly differently as $\mathbf{F}(u) = u^2 \mathbf{v}$. While no explicit exact solution is available, we consider as a reference a high-resolution solution obtained by a fifth order WENO scheme on the 400×400 Cartesian grid, see Chapter 11 of the book [Hesthaven \(2018\)](#) and its supplementary code `BurgersWENO2D.m`. For comparison with our method we choose a first order monotone scheme (Script 7.2 in [Hesthaven \(2018\)](#) and code `BurgersM2D.m`) on the 200×200 Cartesian grid with spacing $h = 0.0025$. Contour lines of the reference solution and the solution by the first order monotone method at time $T = 0.1$ are shown in Figure 6.4(a,b).

We apply our positive meshless scheme with adaptive viscosity (Algorithm 3) on the same Cartesian grid, on a set of 40102 nodes in $[0, 0.5]^2$ obtained by generating $0.5^2/h^2 = 40000$ Halton points in $[0, 0.5]^2$, removing all points with distance less than $0.25h$ from the boundary, and then projecting to the lower and left sides of the boundary the points with distance less than h to them, and on a set of 40091 random nodes in $[0, 0.5]^2$ obtained in a similar manner, with the components of the nodes from MATLAB's pseudo-random number generator. In all three cases the set of nodes in $[0, 0.5]^2$ is extended periodically to a larger domain, and the sets of influence X_i are computed in the extended domain. The parameters of the scheme are chosen in the same way as before, in particular $\Delta t = 0.2h = 5 \cdot 10^{-4}$ and $\mu = 0.5h = 1.25 \cdot 10^{-3}$.

The contour lines of the solutions at time $T = 0.1$ obtained by our method on the grid and Halton nodes are presented in Figure 6.4(c,d). In addition, we compare the cross sections of all five solutions for $x_2 = 0.1$ in Figure 6.5, and the errors with respect to the reference solution in Table 6.2. Note that in order to compute the cross sections and contour lines in the case of Halton or random nodes we interpolate the solution on the 200×200 Cartesian grid by the piecewise linear polynomial on the Delaunay triangulation of the nodes. The results of the meshless scheme on the grid, Halton and random nodes are very similar, and significantly better than those of the monotone scheme. This is clear from the errors in the table and zoom-in plots in Figure 6.5(c-n). In particular, these results confirm remarkable robustness of our method with respect to the use of scattered points. Note that the contours in Figure 6.4(d) appear wobbling at the shocks, due to the irregular distribution of the Halton nodes in close proximity of the shock lines.

Finally, Figure 6.6 illustrates the performance of our method under refinement. In addition to the Halton points of the previous tests with spacing $h = 0.0025$, we generate three more sets of Halton nodes with $h = 0.01, 0.005$ and 0.00125 , and compute solutions by Algorithm 3. The four plots in Figure 6.6 show the cross-sections of these solutions along with the reference solution and that by the monotone scheme in the vicinity of the same corner as in the plots (e), (i) and (m) of Figure 6.5. These results demonstrate a robust convergence of the solution towards the sharp shocks.

method	E_1 -error	E_2 -error
monotone scheme (Hesthaven (2018) , Script 7.2)	1.21e-02	4.38e-02
meshless scheme (Algorithm 3), Cartesian grid	6.08e-03	2.79e-02
meshless scheme (Algorithm 3), Halton points	5.47e-03	2.71e-02
meshless scheme (Algorithm 3), Random points	6.45e-03	3.34e-02

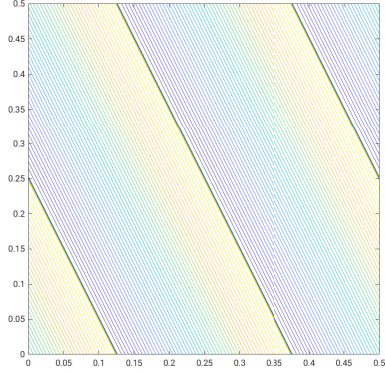
Table 6.2: Example 2: Comparison of the errors (with respect to the reference solution) obtained by a standard monotone scheme on the Cartesian grid, and our meshless method on the Cartesian grid, Halton and random nodes ($T = 0.1$).

6.3. Example 3: Rotating wave

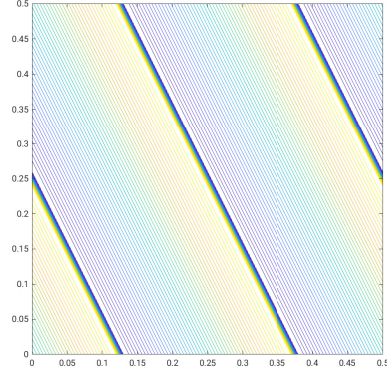
As last example, we consider a more challenging equation with a non-convex flux $\mathbf{F}(u) = (\sin(u), \cos(u))$ on the spatial domain $[-2, 2] \times [-2.5, 1.5]$, with periodic boundary conditions and initial condition

$$u_0(\mathbf{x}) = \begin{cases} 3.5\pi, & \text{if } \|\mathbf{x}\|_2 < 1, \\ 0.25\pi, & \text{otherwise.} \end{cases}$$

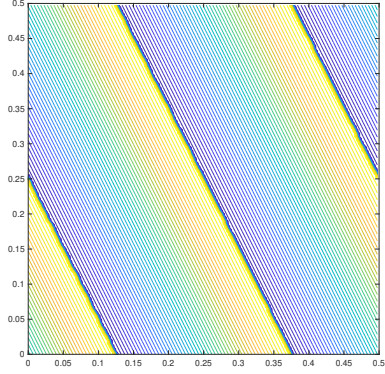
The solution is clearly discontinuous from the beginning, but the shape of the discontinuity curve greatly changes as time advances, making it an excellent test for our adaptive viscosity method. The exact solution



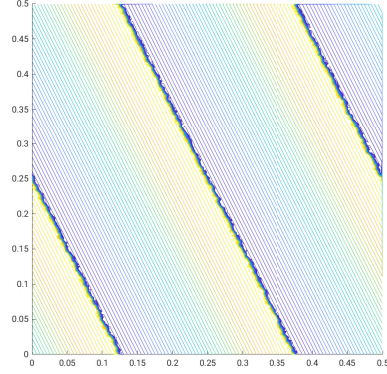
(a) Reference solution.



(b) Monotone scheme, [Hesthaven \(2018\)](#).



(c) Meshless scheme (Algorithm 3) on Cartesian grid.

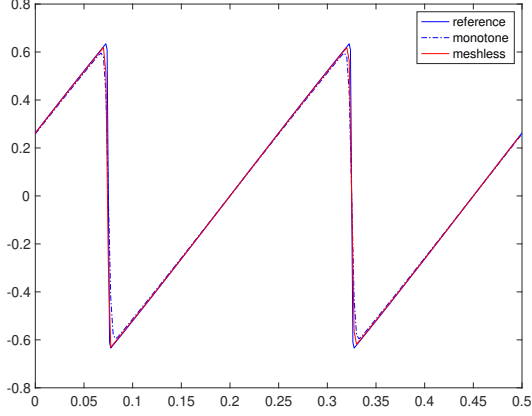


(d) Meshless scheme (Algorithm 3) on Halton points.

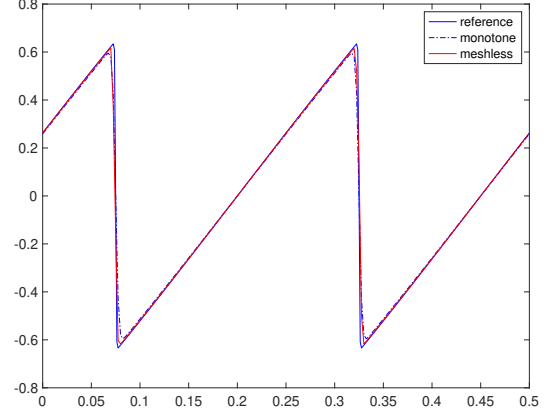
Figure 6.4: Example 2: Comparison of the contours of the numerical solutions with the reference solution ($T = 0.1$).

is not available, but its behavior is well known in the literature, see [Kurganov et al. \(2007\)](#); [Guermond et al. \(2011\)](#); [Guermond and Popov \(2017\)](#); [Hesthaven \(2018\)](#). This test problem has been found challenging for many standard numerical schemes. As a reference, here we use a high-resolution numerical solution obtained by employing the second order central scheme described in [Hesthaven \(2018\)](#), Chapter 10, and the supplementary code `BurgersC2D.m`, on the 1600×1600 Cartesian grid, see Figure 6.7(a).

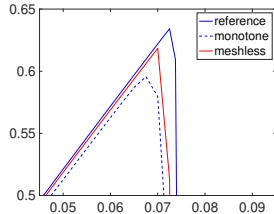
We apply our positive scheme with adaptive viscosity (Algorithm 3) on irregular nodes obtained in the same way as in Example 2 by modifying 400^2 Halton points in $[-2, 2] \times [-2.5, 1.5]$ near the boundaries. This corresponds to the spacing $h = 0.01$, and hence we choose $\Delta t = 0.2h = 2 \cdot 10^{-3}$, $\mu = 0.5h = 5 \cdot 10^{-3}$. The results at $T = 1$ are again compared with the solution obtained by employing the first order monotone scheme of [Hesthaven \(2018\)](#), Script 7.2, on the 400×400 Cartesian grid. Figure 6.7(b,c) compares the solutions at the final time and the corresponding contour lines. The results reproduce the correct shape, with our solution having edges of discontinuity a bit less neat, which is expected having used Halton points. Despite this, Table 6.3 shows that the error with respect to the reference solution obtained with our method is somewhat better. Note that the maximum of the numerical solution is preserved at the same value 3.5π up to machine precision at all time steps. Finally, Figure 6.8 shows the detected fault points and the distribution of the viscosity values at the final time, indicating that viscosity is applied near the shocks as



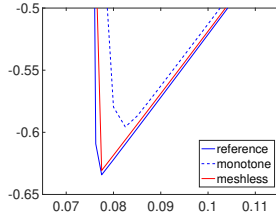
(a) Meshless scheme on Cartesian grid.



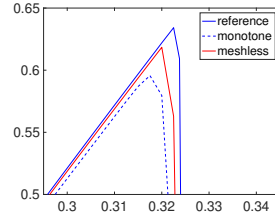
(b) Meshless scheme on Halton points.



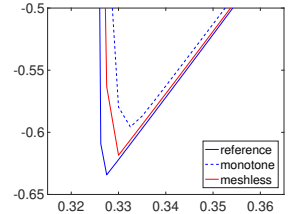
(c) Grid: zoom no. 1.



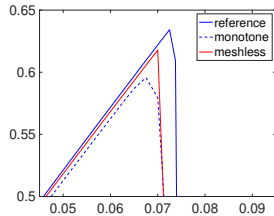
(d) Grid: zoom no. 2.



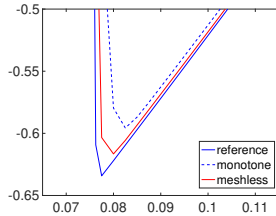
(e) Grid: zoom no. 3.



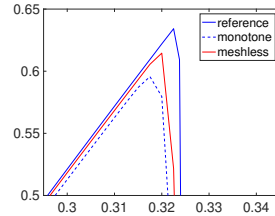
(f) Grid: zoom no. 4.



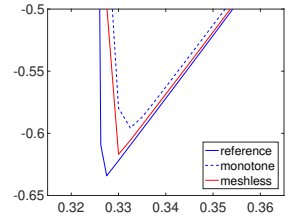
(g) Halton: zoom no. 1.



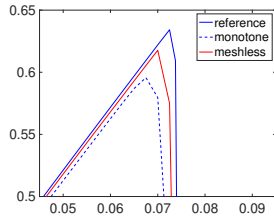
(h) Halton: zoom no. 2.



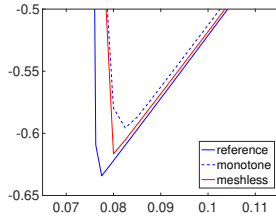
(i) Halton: zoom no. 3.



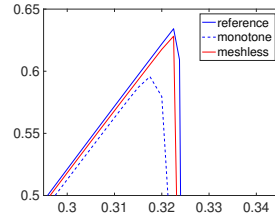
(j) Halton: zoom no. 4.



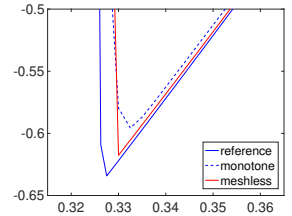
(k) Random: zoom no. 1.



(l) Random: zoom no. 2.



(m) Random: zoom no. 3.



(n) Random: zoom no. 4.

Figure 6.5: Example 2: Comparison of the cross sections at $x_2 = 0.1$ of the reference solution and the monotone scheme with the meshless scheme of Algorithm 3 on (a) the Cartesian grid and (b) Halton points ($T = 0.1$). Subfigures (c)–(n) show zoom-in plots of four critical portions of the cross sections near the shocks, comparing three meshless solutions (on the Cartesian grid, Halton and random points) to the reference solution and the solution by the monotone scheme.

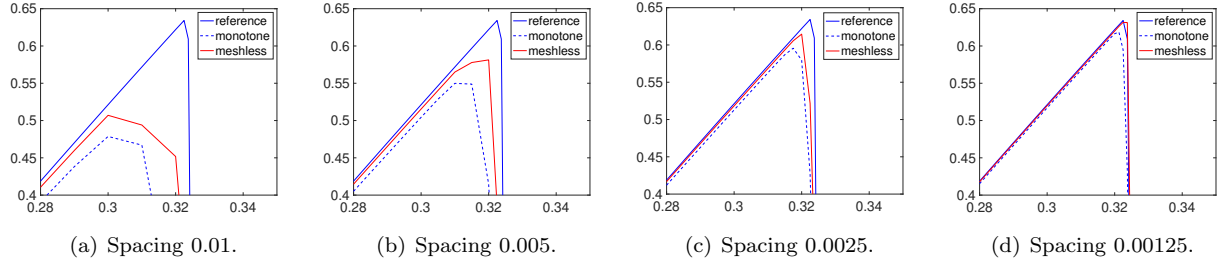


Figure 6.6: Example 2: Comparison of the cross sections at $x_2 = 0.1$ of the reference solution and the monotone scheme with the meshless scheme of Algorithm 3 on Halton points ($T = 0.1$) with decreasing spacing in the vicinity of the same corner as in the plots (e), (i) and (m) of Figure 6.5.

intended.

method	E_1 -error	E_2 -error
monotone scheme (Hesthaven (2018), Script 7.2)	7.38e-03	3.76e-02
meshless scheme (Algorithm 3), Halton points	6.51e-03	2.93e-02

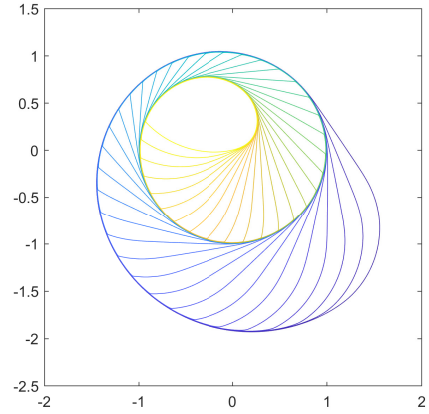
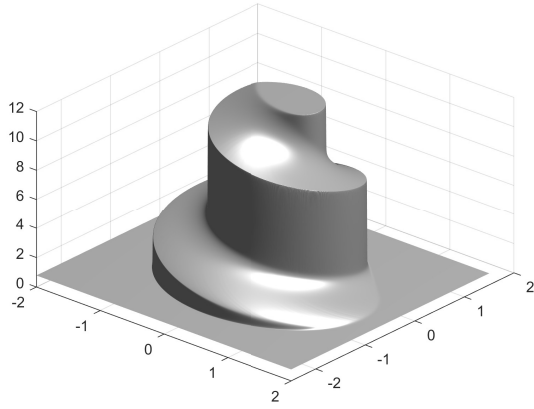
Table 6.3: Example 3: Comparison of the errors (with respect to the reference solution) obtained by a standard monotone scheme on the Cartesian grid, and our meshless method on Halton points ($T = 1$).

7. Conclusion

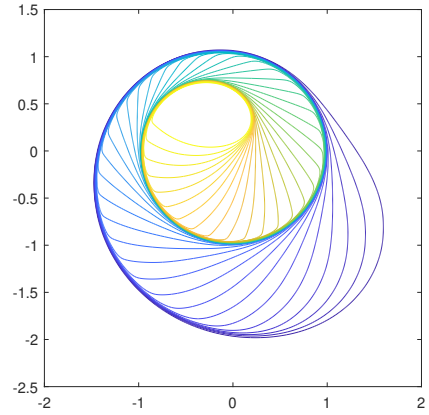
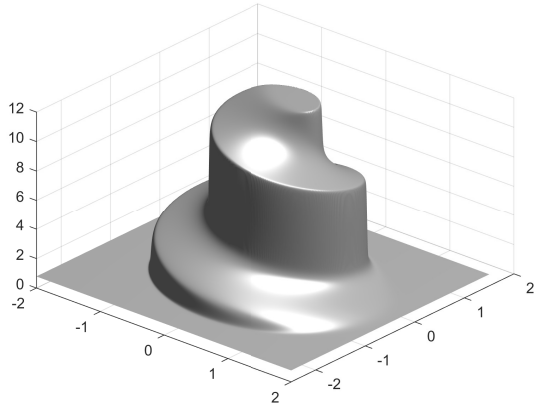
We propose a positive scheme for multivariate scalar conservation laws based on a purely meshless finite difference discretization in space, explicit Euler time stepping and locally varying artificial viscosity. To obtain the scheme, we modify the ℓ_2 -minimal numerical differentiation formulas of Davydov and Schaback (2018) by inequality constraints, and apply them to the directional derivatives arising from the quasilinear form of the conservation law as well as to the Laplace operator that defines artificial viscosity. Coupling of the two numerical differentiation formulas and adaptive selection of the sets of influence allows to meet a local CFL condition without any *a priori* time step restriction. Moreover, we suggest adaptive selection of the amount of local artificial viscosity by applying the fault detection method of Bracco et al. (2019). This is possible in particular because the positivity and hence stability of the scheme is achieved without relying on the artificial viscosity term, whose sole purpose is therefore the shock capturing.

Numerical experiments for bivariate benchmark test problems confirm the robust performance of the method on irregular nodes and advantages of adaptive artificial viscosity. The accuracy of the obtained solutions is comparable to if not better than that for standard monotone methods available only on Cartesian grids.

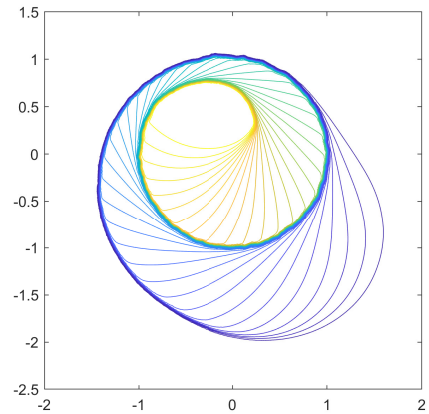
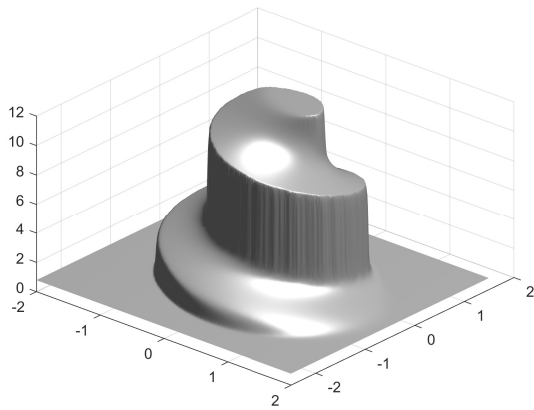
There are many directions of research of interest for future work. Purely polynomial numerical differentiation may be enhanced by kernel-based techniques that are used successfully in the meshless finite difference methods of RBF-FD type, see Fornberg and Flyer (2015); Davydov and Schaback (2016); Bayona et al. (2017); Davydov and Schaback (2019). The flexibility of the space discretization makes it natural to explore in this setting the local time-stepping combined with local refinement in space. Positive schemes may be used locally where appropriate, enhanced by high order schemes as part of limiter- or ENO/WENO-based algorithms. In particular, an extension to the conservation laws of the meshless FCT method for linear convection dominated problems Sokolov et al. (2019) could be considered. An important goal for future work is the extension of the introduced positive schemes to general vector-valued conservation problems.



(a) Reference solution

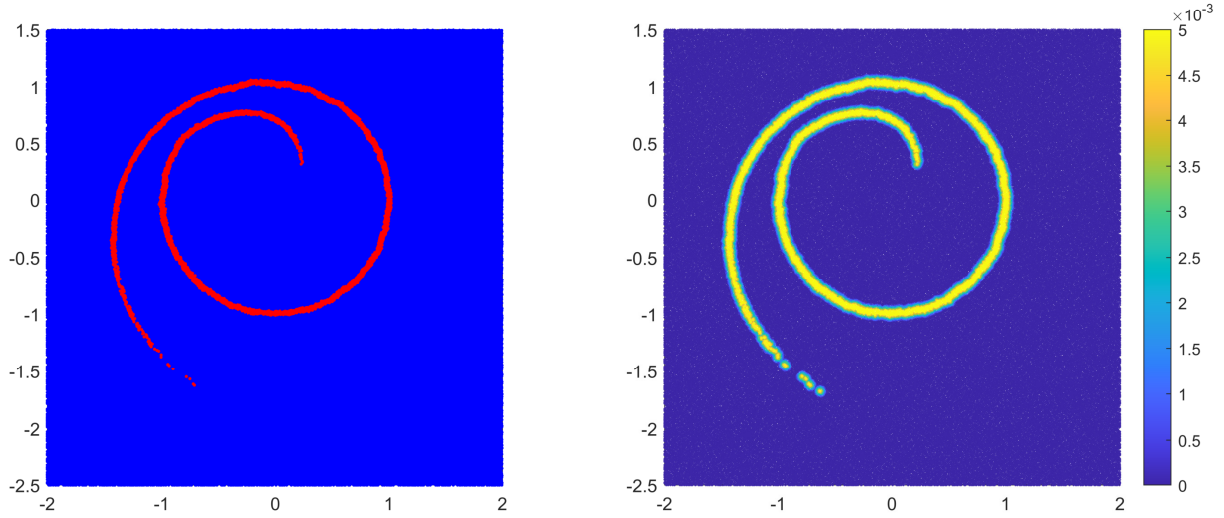


(b) Monotone scheme (Hesthaven (2018), Script 7.2) on Cartesian grid



(c) Meshless scheme (Algorithm 3) on Halton points

Figure 6.7: Example 3: (a) High-resolution reference solution at $T = 1$ and its contour lines. Comparison between the solutions at $T = 1$ by (b) a monotone scheme on the 400×400 Cartesian grid and (c) our positive scheme with adaptive viscosity on $1.602 \cdot 10^5$ irregular points.



(a) Fault points (in red).

(b) Values of μ_i obtained by formula (32).

Figure 6.8: Example 3: Detected fault points and viscosity values at $T = 1$.

Acknowledgments

We thank anonymous reviewers whose comments helped to improve the quality of the paper. C. Bracco, C. Giannelli and A. Sestini are members of the INdAM Research Group GNCS. This work has been partially supported by INdAM through Finanziamenti Premiali SUNRISE and GNCS.

Bibliography

- Batina, J., 1993. A gridless Euler/Navier-Stokes solution algorithm for complex-aircraft applications, in: 31st Aerospace Sciences Meeting, NASA. p. 333.
- Bayona, V., Flyer, N., Fornberg, B., Barnett, G.A., 2017. On the role of polynomials in RBF-FD approximations: II. Numerical solution of elliptic PDEs. *Journal of Computational Physics* 332, 257–273.
- Bracco, C., Davydov, O., Giannelli, C., Sestini, A., 2019. Fault and gradient fault detection and reconstruction from scattered data. *CAGD* 75, 101786.
- Courant, R., Friedrichs, K., Lewy, H., 1928. Über die partiellen Differenzengleichungen der mathematischen Physik. *Mathematische Annalen* 100, 32–74.
- Courant, R., Isaacson, E., Rees, M., 1952. On the solution of nonlinear hyperbolic differential equations by finite differences. *Communications on pure and applied mathematics* 5, 243–255.
- Davydov, O., Schaback, R., 2016. Error bounds for kernel-based numerical differentiation. *Numer. Math.* 132, 243–269.
- Davydov, O., Schaback, R., 2018. Minimal numerical differentiation formulas. *Numer. Math.* 140, 555–592.
- Davydov, O., Schaback, R., 2019. Optimal stencils in Sobolev spaces. *IMA Journal of Numerical Analysis* 39, 398–422.
- Evans, L.C., 2010. *Partial differential equations*. American Mathematical Soc.
- Flyer, N., Lehto, E., Blaise, S., Wright, G.B., St-Cyr, A., 2012. A guide to RBF-generated finite differences for nonlinear transport: Shallow water simulations on a sphere. *Journal of Computational Physics* 231, 4078–4095.
- Fornberg, B., Flyer, N., 2015. *A Primer on Radial Basis Functions with Applications to the Geosciences*. SIAM.
- Fornberg, B., Lehto, E., 2011. Stabilization of RBF-generated finite difference methods for convective pdes. *Journal of Computational Physics* 230, 2270–2285.
- Fürst, J., Sonar, T., 2001. On meshless collocation approximations of conservation laws: Preliminary investigations on positive schemes and dissipation models. *Z. Angew. Math. Mech.* 81, 403–415.
- Ghosh, A., Deshpande, S., 1995. Least squares kinetic upwind method for inviscid compressible flows, in: 12th Computational Fluid Dynamics Conference, American Institute of Aeronautics and Astronautics. p. 1735.
- Guermond, J.L., Nazarov, M., Popov, B., Yang, Y., 2014. A second-order maximum principle preserving lagrange finite element technique for nonlinear scalar conservation equations. *SIAM Journal on Numerical Analysis* 52, 2163–2182.
- Guermond, J.L., Pasquetti, R., Popov, B., 2011. Entropy viscosity method for nonlinear conservation laws. *J. Comput. Phys.* 230, 4248–4267.

- Guermond, J.L., Popov, B., 2017. Invariant domains and second-order continuous finite element approximation for scalar conservation equations. *SIAM J. Numer. Anal.* 55, 3120–3146.
- Hesthaven, J.S., 2018. Numerical methods for conservation laws. SIAM. Supplement: MATLAB code provided at <http://archive.siam.org/books/cs18/>.
- Huh, J.Y., Rhee, J.S., Kim, K.H., Jung, S.Y., 2018. New least squares method with geometric conservation law (GC-LSM) for compressible flow computation in meshless method. *Computers & Fluids* 172, 122–146.
- Jacquemin, T., Tomar, S., Agathos, K., Mohseni-Mofidi, S., Bordas, S., 2020. Taylor-series expansion based numerical methods: A primer, performance benchmarking and new approaches for problems with non-smooth solutions. *Archives of Computational Methods in Engineering* 27.
- Jameson, A., 1995. Analysis and design of numerical schemes for gas dynamics, 1: artificial diffusion, upwind biasing, limiters and their effect on accuracy and multigrid convergence. *International Journal of Computational Fluid Dynamics* 4, 171–218.
- Katz, A., Jameson, A., 2010. Meshless scheme based on alignment constraints. *AIAA journal* 48, 2501–2511.
- Katz, A., Jameson, A., 2012. A comparison of various meshless schemes within a unified algorithm, in: 47th AIAA Aerospace Sciences Meeting including The New Horizons Forum and Aerospace Exposition 2009, AIAA. p. 596.
- Kuhnert, J., 2003. An upwind finite pointset method (FPM) for compressible Euler and Navier-Stokes equations, in: *Meshfree methods for partial differential equations*. Springer, pp. 239–249.
- Kurganov, A., Petrova, G., Popov, B., 2007. Adaptive semidiscrete central-upwind schemes for nonconvex hyperbolic conservation laws. *SIAM Journal on Scientific Computing* 29, 2381–2401.
- Kuzmin, D., 2020. Monolithic convex limiting for continuous finite element discretizations of hyperbolic conservation laws. *Computer Methods in Applied Mechanics and Engineering* 361, 112804.
- Li, P.W., Fan, C.M., 2017. Generalized finite difference method for two-dimensional shallow water equations. *Engineering Analysis with Boundary Elements* 80, 58–71.
- Löhner, R., Sacco, C., Onate, E., Idelsohn, S., 2002. A finite point method for compressible flow. *International Journal for Numerical Methods in Engineering* 53, 1765–1779.
- von Neumann, J., Richtmyer, R.D., 1950. A method for the numerical calculation of hydrodynamic shocks. *Journal of Applied Physics* 21, 232–237.
- Oñate, E., Idelsohn, S., Zienkiewicz, O., Taylor, R., 1996. A finite point method in computational mechanics. applications to convective transport and fluid flow. *International journal for numerical methods in engineering* 39, 3839–3866.
- Ortega, E., Oñate, E., Idelsohn, S., 2009. A finite point method for adaptive three-dimensional compressible flow calculations. *International journal for numerical methods in fluids* 60, 937–971.
- Praveen, C., Deshpande, S., 2007. Kinetic meshless method for compressible flows. *International journal for numerical methods in fluids* 55, 1059–1089.
- Seibold, B., 2008. Minimal positive stencils in meshfree finite difference methods for the Poisson equation. *Comput. Methods Appl. Mech. Eng.* 198, 592–601.
- Seifarth, T., 2017. Numerische Algorithmen für gitterfreie Methoden zur Lösung von Transportproblemen. Ph.D. thesis. University of Kassel.
- Shankar, V., Fogelson, A.L., 2018. Hyperviscosity-based stabilization for radial basis function-finite difference (RBF-FD) discretizations of advection–diffusion equations. *Journal of Computational Physics* 372, 616–639.
- Shu, C., Ding, H., Chen, H., Wang, T., 2005. An upwind local RBF-DQ method for simulation of inviscid compressible flows. *Computer Methods in Applied Mechanics and Engineering* 194, 2001–2017.
- Sokolov, A., Davydov, O., Kuzmin, D., Westermann, A., Turek, S., 2019. A flux-corrected RBF-FD method for convection dominated problems in domains and on manifolds. *Journal of Numerical Mathematics* 27, 253–269.
- Sridar, D., Balakrishnan, N., 2003. An upwind finite difference scheme for meshless solvers. *Journal of Computational Physics* 189, 1–29.
- Suchde, P., Jacquemin, T., Davydov, O., 2022. Point cloud generation for meshfree methods: An overview. *Archives of Computational Methods in Engineering* .
- Tominec, I., Nazarov, M., 2023. Residual viscosity stabilized RBF-FD methods for solving nonlinear conservation laws. *Journal of Scientific Computing* 94, 14.
- Yin, L., Shen, L., Lv, G., 2011. Five-point positive meshless scheme for hyperbolic conservation laws. *International Journal for Numerical Methods in Biomedical Engineering* 27, 619–631.
- Zhang, X., Xia, Y., Shu, C.W., 2012. Maximum-principle-satisfying and positivity-preserving high order discontinuous Galerkin schemes for conservation laws on triangular meshes. *Journal of Scientific Computing* 50, 29–62.